



ACORDE: A new application for estimating the dose absorbed by passengers and crews in commercial flights

Hernán Asorey^{a,b,*}, Mauricio Suárez-Durán^{c,d}, Rafael Mayo-García^e

^a Medical Physics Department, Comisión Nacional de Energía Atómica, Centro Atómico Bariloche, Av. E. Bustillo 9500, San Carlos de Bariloche, 8400, Río Negro, Argentina

^b Instituto de Tecnologías en Detección y Astropartículas (ITeDA), Comisión Nacional de Energía Atómica, Centro Atómico Constituyentes, Av. Gral. Paz 1499, Villa Maipú, 1650, Buenos Aires, Argentina

^c Université Libre de Bruxelles (ULB), Boulevard du Triomphe 155, Ixelles, 1050, Brussels, Belgium

^d Universidad de Pamplona, Km 1 Vía Bucaramanga Ciudad Universitaria, Pamplona, 1050, Norte de Santander, Colombia

^e Centro de Investigaciones Energéticas Medioambientales y Tecnológicas (CIEMAT), Av. Complutense 40, Madrid, 28040, Madrid, Spain

ARTICLE INFO

Keywords:

Cosmic rays
Onboard dose calculation
Commercial flights

ABSTRACT

Atmospheric radiation produced during the interaction of cosmic rays with the atmosphere could be considerably high at typical flight altitudes and constitutes a risk factor for people and avionics onboard the plane. In this work, we present ACORDE, a Monte Carlo-based method to estimate the dose during a commercial flight by using state-of-the-art simulation codes and considering the course travelled, the real-time atmospheric and geomagnetic conditions, and a model of the plane and an anthropomorphic phantom to obtain the effective dose on a flight-by-flight basis.

1. Introduction

Aircraft crews are considered within the highest exposure annual effective dose (Clarke et al., 1990), as commercial flights take place at altitudes over 10 km a.s.l., which results into a much larger exposure to environmental ionising radiation than at ground level. This radiation, usually known as atmospheric radiation, is produced by the interaction between cosmic rays and the nucleus of the molecules composing the Earth's atmosphere. Studies show that exposure to these radiation can increase the risk factor of radiation-sickness, as is the case with crew members and passengers (Sanlorenzo et al., 2015), and radiation damage in the electronics onboard the aircraft (avionics) (Dyer and Lei, 2001). Since the 90's, several projects and initiatives have been carried out tending to measure and estimate the effective dose that a person will receive during different type of flights due to the atmospheric radiation (Paretzke and Heinrich, 1993; Schrewe, 1999), as for example, the measurement of onboard radiation by using silicon planar detectors finding lower limits for the dose rates values in the range 1.4–3.2 $\mu\text{Sv h}^{-1}$ (Beaujean et al., 1999). These kind of works engage several governments to revise their national radiation protection laws by the 00's decade pointing to consider the increased atmospheric radiation at flight altitude as occupational risks, as it is clearly stated by Schrewe (1999). By 2004, different reports from working

groups brought together comparative analysis between different calculation codes and specific measurement campaigns, aiming to provide datasets for assessing individual doses and the validity of different approaches (Lindborg et al., 2004), and motivating the publication of revised safety standards including the exposure to natural sources of ionising radiation as occupational exposure (Bartlett, 2004).

As it will be detailed in the next section, at flight altitudes the dose received due to the atmospheric radiation could reach rates of up to 5 $\mu\text{Sv h}^{-1}$, attributed to photons, electrons and positrons (~25%), protons (~15%), muons (~5%) and neutrons ($\geq 55\%$) (Bartlett, 2004). Given the impact of neutrons for the dose calculation, several specific measurements of the neutron flux at flight altitudes have been conducted. In particular, Vuković et al. (2010) installed track etch detectors with a boron foil converter covering different European and transatlantic routes in northern geographical latitudes from 21° to 58° in secular conditions of the geomagnetic field and obtained average ambient equivalent dose rates ($H^*(10)$) due to neutrons of $H^*(10) = 5.9 \mu\text{Sv h}^{-1}$, while commercial electronic dosimeters gave average values of $H^*(10) = 1.4 \mu\text{Sv}$ during the same flights. Typically, onboard measurement of the non electromagnetic components exceed the capacities of standard radiation detectors extensively used in the industry, such as the Gamma-Scout (Gamma-Scout GmbH, 2022) detectors, that

* Corresponding author at: Medical Physics Department, Comisión Nacional de Energía Atómica, Centro Atómico Bariloche, Av. E. Bustillo 9500, San Carlos de Bariloche, 8400, Río Negro, Argentina.

E-mail address: hernanasorey@cnea.gob.ar (H. Asorey).

<https://doi.org/10.1016/j.apradiso.2023.110752>

Received 28 November 2022; Received in revised form 10 February 2023; Accepted 26 February 2023

Available online 2 March 2023

0969-8043/© 2023 The Authors. Published by Elsevier Ltd. This is an open access article under the CC BY-NC-ND license (<http://creativecommons.org/licenses/by-nc-nd/4.0/>).

are only sensitive to the electromagnetic and alpha radiation. More recently, Ambrožová et al. (2020) carried out the REFLECT (REsearch FLight of EURADOS and CRREAT) research camping by installing more than 20 different type of new and commonly used radiation detectors and dosimeters placed onboard in a small aircraft during a single flight that started and ended at the Vaclav Havel Airport in Prague, and flew during 90 min at an altitude of 39,000 ft (flight level FL390). One of the main conclusions from the REFLECT study is that conventional neutron detectors tends to underestimate the dose as they are not sensitive to high-energy neutrons. Moreover, they also conclude that additional characterisation would be required on some commonly used instruments, as they were specifically designed to measure only part of the components of the atmospheric radiation and were not primarily intended for their use in a very complex mixed radiation field and with much wider energy ranges such as the observed in the atmospheric radiation at flight altitudes (Ambrožová et al., 2020).

Therefore, for now the exposure to ionising radiation in a flight-by-flight basis can only be estimated by using physical models trying to reproduce the evolution of the interaction between the cosmic rays and the atmosphere under different conditions. Different approaches have been used for this tasks. On the one hand, some tools are based on different cosmic rays and extensive air showers semi-analytical models, i.e., models that use pre-calculated libraries, interpolate and/or extrapolate atmospheric conditions along a predefined and theoretical route, and finally several types of corrections, such as those associated with space weather phenomena, can be applied to obtain the expected dose onboard the aircraft. The Nowcast of Atmospheric Ionising Radiation for Aviation Safety (NAIRAS) model (Mertens et al., 2013, 2010) and the well known and extensively used CARI7/CARI7-A codes (Copeland, 2017) are good examples of those. Then, the usage of pre-compiled libraries largely reduces the computing times, but cannot cover all the complexities associated with the physics mechanisms involved.

Monte Carlo based codes, on the other hand, require much larger computing resources, but are able to properly handle larger complexity levels. Early attempts, such as the original work by Roesler et al. (2002), calculated the expected flux of atmospheric radiation \bar{E} under secular and a discrete set of solar modulation parameters at flight altitudes, by using an own designed code based on FLUKA (Battistoni et al., 2015). The main part of these codes tries to calculate the development of the so called Extensive Air Shower (EAS), a cascade of different types of secondary particles that are produced when a cosmic rays interact with the atmosphere via radiative and decay processes that propagate towards the ground following approximately the CR direction (Grieder, 2010). Hence, the atmospheric radiation is the complete population of surviving secondary particles that were produced during interaction of the integrated cosmic ray flux with the air and that are present at a given altitude. Another important part of the Monte Carlo codes are devoted to the calculation of shielding produced by the building materials of the aircraft and the consequent energy that the secondaries deposit over different type of tissues.

During the last decades, the enhancement of computational power and the improvement of new tools to model EAS, such as CORSIKA (Heck et al., 1998; Engel et al., 2019), and the interaction of radiation with matter, e.g., Geant4 (Agostinelli et al., 2003), offer very precise calculation of atmospheric radiation as a function of the altitude under different geomagnetic (Asorey et al., 2018) and atmospheric conditions (Grisales-Casadiegos et al., 2022; Rubio-Montero et al., 2021a), which requires considerable computational capabilities. Likewise, current facilities as cloud-based and high performance computing infrastructures open the door to increasing the precision in the dose calculation along commercial flights (Rubio-Montero et al., 2021b). In this paper, we show the integration of the former enhancements in an automatized framework called ACORDE (Application CODE for the Radiation Dose Estimation). In Section 2, we introduce the details of how the flux of cosmic rays is calculated along real commercial flight routes, i.e., for a given set of geographical positions and taking

into account the atmospheric conditions and the geomagnetic field. It also presents how is it possible to obtain a precise estimation of the cosmic radiation for each geographical position having used an accurate atmospheric profile at each position. Within this section, a realistic model of the airplane fuselage and an anthropomorphic water-based phantom are also described as well as how ACORDE determines the total effective dose along the route from the secondary flux of particles. Then, in Section 3, a systematic study of the integrated effective dose calculated with ACORDE in more than 300 flights that have taken place during 2021 and 2022, and a comparison with the doses obtained by using current available methods is also included. With the aim of easing a quality check of the new ACORDE methodology and its precision, results of the effective dose with and without the hadronic and muonic components of the EAS are also presented for some selected flights. In these calculi, the expected values of radiation that commercial radiation counters would provide are shown, showing that there is a significant increase in the effective dose if all the radiative components would be actually estimated, as ACORDE does. Finally, in Section 4 the main conclusions of this work and the future perspectives in the development of ACORDE are presented.

2. Methods

2.1. Modelling of extensive air showers

Cosmic rays (CRs) are defined as particles and atomic nuclei coming from outside the Earth which cover a range of energies from a few GeVs up to $>10^{20}$ eV (Blümer et al., 2009). Once these cosmic rays reached the top of the atmosphere (~ 100 km a.s.l.), their interaction with the elements there presented produced an EAS, as Rossi and Auger discovered in the 1930's (Kampert and Watson, 2012). The development and properties of an EAS depend on the energy (E_p) and composition (i.e., gamma, proton, iron, etc.) of the incident CR and could reach a maximum production of up to 10^{10} particles at the highest energies. The point at which this maximum takes place is named X_{\max} and it is measured in atmospheric depth X , typically expressed in units of g cm^{-2} (The Pierre Auger Collaboration, 2012). The distribution of secondaries density is well described by the Nishimura–Kamata–Greisen (NKG) lateral distribution function (LDF) in terms of the distance r from the EAS axis, i.e., the direction pointed by the initial momentum of the CR (Greisen, 1960).

There are two types of EAS that are defined by the nature of the initial CR: Electromagnetic (EM) showers and hadron-initiated showers. The former are initiated by photons or electrons and most of the processes are mediated by QED interactions, while the later produce hadrons and mesons via fragmentation and hadronization of the resulting fragments. This hadronic component is located in a region near the shower axis and it is dominated by neutrons and protons. This feature is due to the reduced transference of transverse momentum originated in the characteristic leading particle effect of hadronic interactions, see e.g. (Matthews, 2005). In particular, the neutrons are the only quasi-stable neutral hadrons present in the cascade,¹ no ionisation or radiative process affect their propagation in the atmosphere, and are produced by spallation processes of protons on ^{14}N and other nuclei in the atmosphere (Silberberg and Tsao, 1990; Goldhagen, 2003). Due to the development of the EAS, at flight altitudes the hadronic component will not be fully developed and so the contribution of the hadronic component at these altitudes will be much more relevant than at ground level. The reader is referred, for example, to Matthews (2005) and Asorey and Mayo-García (2022) for a complete description of the EAS development.

¹ It is possible to consider neutrons as quasi-stable particles since their lifetime is several orders of magnitude larger than the characteristic time of the cascade evolution.

EAS simulation is a computational demanding task not only because of the physical interactions to be modelled but also of the large number of particles that are tracked, up to $\sim 10^{10}$ at the higher values of E_p . Several tools are available to perform this type of simulation, but CORSIKA (Heck et al., 1998) is the most widespread and validated, and it is being continuously upgraded (Engel et al., 2019). This software simulates the EAS produced by a single CR by setting parameters such as the atmospheric model, the local components of the geomagnetic field, or the altitude of the observation level. This means that calculating the expected background radiation at any geographical position and time by using CORSIKA, requires an external tool that sets the aforementioned parameters in a dynamic way. This latest because the local atmospheric profile changes along the year and the flux of CRs is affected by the Solar activity, which in turn affects the geomagnetic field.

The Latin American Giant Observatory (LAGO) (Sidelnik et al., 2017) has designed and developed ARTI (Sarmiento-Cano et al., 2021) a public accessible toolkit that automates not only the calculation and analysis of the background radiation, but also the estimation of the response of its detectors to this type of radiation (Asorey et al., 2022a). ARTI allows the estimation of the expected cosmic radiation at any geographical position (Sarmiento-Cano et al., 2019) under realistic and time-evolving atmospheric and geomagnetic conditions (Asorey et al., 2018; Grisales-Casadiegos et al., 2022; Rubio-Montero et al., 2021a), integrating and articulating CORSIKA, Magneto-Cosmics (Desorgher et al., 2003) and Geant4 (Agostinelli et al., 2003), and including its own analysis package (Sarmiento-Cano et al., 2022). ARTI results have been contrasted and verified through different experiments and measurements at different astroparticle observatories, as most of them take advantage of the atmospheric muon background for the detector calibration, and is has been used in multiple applications in muography, underground labs and safeguard (Rubio-Montero et al., 2021b; Sarmiento-Cano et al., 2021, 2019; Asorey et al., 2015; The Pierre Auger Collaboration, 2020b; Galindo et al., 2017; Peña-Rodríguez et al., 2021; The Pierre Auger Collaboration, 2020a; Peña-Rodríguez et al., 2022; Taboada et al., 2022; Vázquez-Ramírez et al., 2020; Vesga-Ramírez et al., 2021; Vázquez-Ramírez et al., 2021; Bertolli et al., 2022; Sidelnik et al., 2020a,c,b).

To calculate the expected flux Ξ of the atmospheric radiation at any geographical position requires of long integration times in order to avoid statistical fluctuations (Sarmiento-Cano et al., 2022; Asorey et al., 2015). This is because a single EAS involves the interaction and tracking of billions of particles during the shower development along the atmosphere, but the atmospheric radiation is caused by the interaction of up to billions of CR impinging the Earth each second. For the modelling of EAS, not only the interactions involved but also the corresponding atmospheric profile at each location that also varies as a function of time should be considered, as it also determines the evolution of the shower (Dawson, 2017). For this reason ARTI is able to handle different atmospheric available models. Finally, Ξ is also affected by the variable conditions of the heliosphere and the EMF, as both affect the CR transport up to the atmosphere. As developed and described by Asorey et al. (2018), ARTI also incorporates modules to consider changes over the secular magnitude of the EMF and disturbances due to transient solar phenomena, like Forbush decreases.

Once the primary spectra, the atmospheric profile, and the secular and possible disturbances of the EMF are set, it is possible to obtain Ξ by calculating and injecting in the top of the atmosphere the integrated flux of primaries with energies in the range $Z \times \min(\mathcal{R}) < E/\text{eV} < 10^{15}$, where \mathcal{R} is the local directional rigidity cutoff tensor at this place and Z is the charge of the injected primary from protons to irons, $1 \leq Z \leq 26$, that are expected during the integration time τ and in an area of typically 1 m^2 . The complete evolution of each resulting EAS is followed down to the lowest possible kinetic energy of the secondary

particles in CORSIKA.² Once the atmospheric simulations end, all of those secondaries produced by geomagnetically forbidden primaries are removed by comparing the magnetic rigidity of the parent primary with the time evolution of the local directional rigidity cutoff tensor \mathcal{R} . The reader is referred to Asorey et al. (2018) for a complete and detailed explanation of all these steps.

As mentioned in Section 1, all these processes at this level of detail require of large computing capacity. As an example, to estimate the flux Ξ of the expected secondary particles per square meter per day for a high-latitude site it is required to compute the development of $\sim 10^9$ EAS, and producing a similar number of secondaries at ground level. ARTI is prepared for running on both high performance computing (HPC) clusters and Docker containers executed on virtualized cloud-based environments, such as the European Open Science Cloud (EOSC), and is capable to store and access the produced data catalogues at public and federated cloud storage servers (Rubio-Montero et al., 2021b).

In the next subsection we will show how it is possible to take advantage of all the capabilities of ARTI to perform a precise estimation of the cosmic radiation expected along the real track of a commercial route.

2.2. ACORDE

In view of all the above described functionalities, by using ARTI we are able to precisely calculate the expected flux of atmospheric radiation at any place in the World and under real-time atmospheric and geomagnetic conditions, and at any altitude above the Earth's surface (Sarmiento-Cano et al., 2022).

As mentioned in Section 2.1, ARTI has been extensively used and tested in a large variety of astroparticle experiments and technological applications. Based on these experiences and the good agreement observed between the calculated flux of radiation and the different experiments performed to validate this simulation framework, we extended ARTI functionalities to develop ACORDE (*Application CODE for the Radiation Dose Estimation*), a framework allowing the automatic and unsupervised calculation of the expected integrated dose that a person will receive during a commercial flight along the plane course. The main difference of ACORDE when compared with existing methods to determine onboard doses, is that ACORDE performs dedicated and intensive Monte Carlo simulations of the interaction of radiation with matter to determine, on a flight-by-flight basis, a realistic estimation of the secondary radiation expected at each selected point of the flight track; and the interaction of this secondary radiation with the aircraft and the human tissues to get the corresponding doses. For these reasons, ACORDE is specifically designed to take advantage of running on high performance computing (HPC) clusters operating with SLURM (Yoo et al., 2003) or other commonly used workload managers, and in Docker (Merkel, 2014) containers running on virtualized public or federated cloud-based environments such as the Amazon Web Services (AWS) or the European Open Scientific Cloud (EOSC) (Rubio-Montero et al., 2021b).

The ACORDE workflow is divided into four consecutive steps:

1. obtaining and segmenting the flight track along its route;
2. extracting the atmospheric profile and determining the geomagnetic conditions for each track segment;
3. simulating the secondary flux of particles in the observed conditions of each track; and

² Currently, for CORSIKA v7.7402 compiled with GHEISHA for the low energy interaction models (Fesefeldt, 1985), these values are $E_n = 50 \text{ MeV}$ for hadrons (except neutral pions π^0), $E_\mu = 10 \text{ MeV}$ for muons, and $E_{e^\pm} = E_{\gamma, \pi^0} = 50 \text{ keV}$ for electrons, photons and π^0 (Heck and Pierog, 2020).

4. simulating the shielding effect of the aircraft fuselage and the corresponding effective dose over an anthropomorphic phantom model, and/or a radiation detector on board the plane.

In the industry, each commercial flight is unambiguously identified by an alphanumeric code commonly known as flight number, flight code, or flight designator, which consists of a two-character airline designator followed by a 1 to 4 digit number. ACORDE identifies each calculated flight by joining the flight designator and an 8-digit number for the date flight (YYYYMMDD), such as for example, the flight from Madrid (ES) to Buenos Aires (AR) operated by Iberia Líneas Aéreas de España, S. A., or just Iberia (IB), that took place on Fri, Jun 10th, 2022, is internally coded in ACORDE as IB6845_20220610. Once the flight is correctly identified, ACORDE checks for its existence in several public databases and obtains the corresponding flight course track and all the publicly available data of the flight. Most online databases grant public access to the tracks for up to 90 days after the flight. However, commercial services provide private access for up to 3 years from the flight date.³ Finally, all the gathered information is packed into a JSON file (IB6845_20220610.json) and stored in its own database for future reference.

Once the file containing the recorded track is gathered, the relevant information is obtained from a first analysis of the track, such as the arrival and departure airports and times, or the aircraft model. Then, the path is divided into three main stages: takeoff, cruise, and landing. Takeoff takes place between the time of the lift-off t_0 (provided) and up to the start of the cruise (not provided). The landing phase starts when the cruise ends (also not provided) and it is over at the moment of the touch down t_f (also provided). Then, the cruise phase is automatically determined by ACORDE by analysing the recorded altitudes and their first time derivative. Immediately after the starting and ending times for the cruise are derived, the three stages of the flight are determined as well as the total duration of each one: Δt_t , Δt_c and Δt_l for the takeoff, cruise and landing respectively, and so, the duration of the flight $\Delta t = t_f - t_0 = \Delta t_t + \Delta t_c + \Delta t_l$. It is important to notice that aircraft operations at the origin and destination airports are not considered since these periods do not impact the total radiation exposure directly related to the flight.

The analysis of the track continues by defining N waypoints of the track, with N depending on the total duration of the flight, Δt . Each waypoint is defined by a four-dimensional vector $\vec{r}_i = (\phi_i, \lambda_i, h_i, t_i)$, where ϕ_i , λ_i , h_i and t_i are the geographic coordinates (latitude, longitude and altitude above sea level) and the UTC time of the i -esim waypoint. The first, \vec{r}_1 , and last, \vec{r}_N , waypoints are defined at the middle point of the takeoff and landing stages, i.e., $t_1 = t_t = t_0 + \Delta t_t/2$ and $t_N = t_l = t_f - \Delta t_l/2$ respectively. The second, \vec{r}_2 , and the penultimate, \vec{r}_{N-1} waypoints corresponds to the beginning and ending of the cruise stage of total duration given by $\Delta t_c = t_{N-1} - t_2$. The cruise is then divided in segments of $\Delta t_i = t_{i+1} - t_i \approx 600; 900$ or 1800 seconds of duration for flight durations of up to 2 h (short flights), 4 h (intermediate flights) or >4 h (long flights) respectively. The exact duration of each step is then approximated by looking forward on having an integer total number of segments during the cruise. Each of these segments could be subdivided again if a change in the cruise altitude $\Delta h_i = h_{i+1} - h_i > 1,500$ ft is observed during each particular step. Instead, if $\Delta h_i \leq 1,500$ ft, the altitude is fixed to the value where the flight stay more time during this segment. In case of doubt, it is always assumed $\Delta h_i = \max(h_{i+1}, h_i)$. Additionally, there are some moments where the actual time difference between two consecutive tracked points can be longer than the corresponding expected value for Δt_i , such as when the aircraft is flying above large unpopulated areas, or over the ocean and far from the continental shores or islands, or near to the poles. In those particular cases, the track is completed by assuming

an orthodromic (great-circle) track between the recorded extrema of these intervals, and then it is segmented using the same algorithm as for the recorded track. The altitude of the interpolated segments (it could be more than one) is fixed to the highest altitude between the two recorded values to always calculate the dose in the worst case scenario. The speed is calculated as the average speed for all the untracked distance along the orthodromic track. Depending on the total duration of the flight Δt , the track could consist of up to $N \gtrsim 35$ waypoints for the longest cases using the default ACORDE configuration: 1 waypoint for each the takeoff and landing stages, plus $(t_c/\Delta t_i) + 1$ for the cruise stage lasting t_c . As mentioned, Δt_i is slightly adjusted from the default configuration for having an integer number of segments. The dose is then calculated along the $(N - 3)$ segments between the waypoints at \vec{r}_i and \vec{r}_{i+1} with durations Δt_i for $i \in [2, N - 1]$ (cruise) and for the takeoff and landing segments with durations $\Delta t_1 = t_1 - t_0$ and $\Delta t_{N-1} = t_{N-1} - t_f$ respectively, and assuming the corresponding characteristics of these segments are those at \vec{r}_1 and \vec{r}_N . ACORDE also produces a .DEG file containing the same waypoints for the flight but in the format requested by the CARI7-A code, that will be used as the dose reference for each flight (see page 32 of (Copeland, 2021)).

Once the waypoints have been obtained and the track has been segmented, the local atmospheric profile corresponding to each waypoint \vec{r}_i for that particular moment t_i is extracted from the Global Data Assimilation System (GDAS) database (NOAA Air Resources Laboratory (ARL), 2004). The Linsley's atmospheric model assumes the atmosphere is a mixture of N_2 (78.1%), O_2 (21.0%), and Ar (0.9%) and it is divided into 5 consecutive layers (National Aerospace Administration (NASA) et al., 1976). In the lower four of them, the density varies exponentially with the altitude h , and so the mass overburden $X(h) = g \int_{\infty}^h \rho(z) dz$, typically in units of $g\text{ cm}^{-2}$, is given by $X(h) = a_l + b_l \exp(-h/c_l)$ for $l = 1 \dots 4$. For the fifth layer, typically for altitudes $h_5 \gtrsim 100$ km, it is assumed a linear variation with the altitude, $X(h) = a_5 - b_5 h/c_5$ that goes up to the altitude where $X(h) = 0$, typically reaching altitudes $h \gtrsim 110$ km above sea level. The Linsley's coefficients at each waypoint $a_{l,i}$, $b_{l,i}$ and $c_{l,i}$, for $l = 1 \dots 5$ are obtained by fitting the atmospheric density profile extracted from GDAS as explained in Grisales-Casadiegos et al. (2022). In this way, we assure to work with the most accurate atmospheric model possible within a 3-hour range containing t_i from the actual passage of the aircraft through \vec{r}_i . By the same way, we obtain the secular values of the Earth's magnetic field at \vec{r}_i by using the current model of the International Geomagnetic Reference Field (IGRF) version 13 (Alken et al., 2021b). Local conditions and transient space weather phenomena that could affect the secular conditions of the geomagnetic field at \vec{r}_i are also considered by accounting for the disturbances of the geomagnetic field and including the local geomagnetic rigidities and the effect of the Earth's magnetic umbra and penumbra using the method developed and described in Asorey et al. (2018). By following this method we are able to determine whether a simulated primary should or should not impinge in the atmosphere producing a shower, depending on its rigidity $R = Z\sqrt{E^2 - m^2}$, where Z , E , and m are the charge, total energy, and mass of the primary particle respectively. It is assumed in these calculations that the altitude, geomagnetic and atmospheric conditions remain constant through the duration Δt_i of each segment.

Given the stochastic nature of the development of the EAS, which is also represented in the Monte Carlo simulations performed to calculate the expected flux of secondary radiation along each segment, it is necessary to limit the effects of fluctuations that could affect or even dominate the radiation background composition estimation. So, the statistical significance of the calculation at each waypoint is increased by artificially enlarging the flight time for each step by the so called "coverage factor" κ of 9, 6, or 3 times for short, intermediate or long flights respectively, totalling a simulation time of 5400 s for each segment. Moreover, due to the Poissonian nature of the background calculations the dose of each segment can be obtained simply

³ See, for example, <https://www.flightradar24.com>

by dividing each calculated dose by κ in the final step of the dose calculation (Sarmiento-Cano et al., 2022).

Once all this information is collected, all the corresponding files are packed and automatically transferred to one of the high performance computing (HPC) centres used for this calculation. The computations are performed inside Docker virtualized environments (Merkel, 2014), the so-called Docker containers or simply containers, that are automatically instantiated and deployed within a physical cluster or a cloud-based virtualized cluster (v-cluster), following the method developed by Rubio-Montero et al. (2021b).

ACORDE computation relies on two different Docker images. The first one, called the ARTI Docker, is devoted to performing the calculations to obtain the expected flux of atmospheric radiation for each segment. Within this container, a pre-compiled instance of CORSIKA (Heck et al., 1998) v7.7402, compiled with QGSJET-II-04 (Ostapchenko, 2011) and GHEISHA (Fesefeldt, 1985) for the high and low energy interaction models respectively, and a specially modified version of the ARTI background simulation framework (Sarmiento-Cano et al., 2022) are included. The third stage starts by deploying one container per track segment, that could sum up to $N - 1$ simultaneous containers allocating the same number of nodes or v-nodes depending on the cluster capabilities. Within each docker, the expected flux of secondary background particles Ξ for each segment located at \vec{r}_i , namely Ξ_i , is calculated for a total integration time $\tau_i = \kappa \Delta t_i$ as explained in Section 2.1. The main result of this third stage of the ACORDE workflow is to produce a single file, the so-called “showers” file (.shw), containing Ξ_i , i.e., all the secondary particles expected at \vec{r}_i , Ξ_i , per square meter during the time τ_i within the considered energy ranges used. Additional analyses are also performed producing, e.g., the lateral distribution functions of the secondary particles, i.e., the normalised particle number and the deposited energy E_d densities per type of secondary as a function of the distance to each shower axis, and the energy spectra of the secondaries per type of particle, as it will showed in Section 3. Each step of the calculation is controlled by customised daemons included in the docker.

The fourth and last stage of ACORDE begins with the deployment of the DOSE docker, devoted for dose calculations. As in the ARTI Docker, a special set of internal daemons controls the execution and reports the advance of the calculation through the different stages. Once the secondaries Ξ_i at \vec{r}_i are obtained, these particles are propagated through a model of the aircraft vessel and an anthropomorphic water-based phantom model, both built in Geant4 (Agostinelli et al., 2003). It is also possible to simulate the integrated dose that should be expected by a Gamma-Scout device (Gamma-Scout GmbH, 2022) located in the cabin to perform comparisons with onboard measurements when corresponds. The aircraft fuselage is simply modelled as a cylinder of 5 meters long and the diameter of the plane in the passenger cabin, i.e., $d = 4.14$ m for the case of the Airbus A320-200 (Airbus, 2020), or 6.09 m for the case of the Airbus A350-900 (Airbus, 2021). As in the real airplane, the fuselage is modelled as a succession of three concentric and hollow cylinders of thickness $r_{e,j} - r_{i,j}$, where r_e and r_i corresponds to the external and inner radius of each hollow j -esim cylinder and the touching condition is obtained simply by doing $r_{i,j} = r_{e,(j-1)}$. Each layer ($j = 0, 1, 2$ for the external coverage, the thermal insulation layer, and the internal coating respectively) was modelled using the corresponding building materials. The cabin is then filled with dry air by considering a cabin altitude of 2000 m a.s.l. (~6,500 ft), and standing in the cabin a simplified anthropomorphic water-based phantom model based on the ICRP-110 Recommendations human phantoms (Clement, 2009) for Geant4 applications (Large et al., 2020) is placed.

It is important to remark at this point that the flux of cosmic rays is isotropic and homogeneous at the relevant energy scale for this calculation. So, even though all the secondary particles produced by the flux of cosmic rays in a given unit area at the top of the atmosphere will be distributed on a much larger surface at flight altitude, a sort of compensation process occurs. As detailed in Sarmiento-Cano et al. (2022), on average a secondary particle that misses the target

area at ground by, say, 10 m to the East, will be compensated by a sib-similar secondary particle originated by a sib-similar primary impinging the upper atmosphere 10 m to the west. So, each secondary particle present in Ξ_i is then propagated from its initial velocity direction by the ACORDE Geant4 application through the aircraft and the anthropomorphic phantom models, and all the relevant interactions, including mini showers that can be produced by the interaction of high energy secondaries with, e.g., the fuselage, are taken into account for the calculation of the absorbed dose within the phantom. So, the deposited energy E_d during the i -esim segment of the track by each secondary particle j , identified in this case by the type of ionising radiation⁴ (R_j), is calculated for each one of the affected organs/tissues (T) of the phantom, and expressed as the absorbed dose ($D_{R_j,T,i}$) in units of gray (Gy, J kg^{-1}). For doing this, we are using the standard procedure for the anthropomorphic reference adult voxelised phantoms (ICRP110Phantoms) included in the Geant4 standard distribution, as described in the International Commission on Radiological Protection (ICRP) publication 110 (Large et al., 2020). As the kind and energy of each particle are known, it is possible also to calculate from $D_{R_j,T,i}$ the equivalent ($H_{T,i}$) for the organ/tissue T , in units of sievert (Sv), by including the radiation weighting factors (w_R) that take account of the relative biological effectiveness (RBE) of the different types of ionising radiations, i.e., $H_{T,i} = \kappa^{-1} \sum_j \sum_{R_j} w_{R_j} D_{R_j,T,i}$, where the summation in j runs over all the secondary particles of the i -esim segment of duration $\Delta t_i = \tau_i/\kappa$. In this sense, $H_{T,i}$ represents the equivalent dose deposited at each organ/tissue by the total flux of secondary particles during the segment i -esim of the track impinging that organ/tissue. As the effective dose E is the main ICRP quantity in terms of radiological protection (Harrison et al., 2021a), E_i is determined from $H_{T,i}$ following the ICRP 103 recommendations (Valentin, 2007; Wrixon, 2008), i.e., $E_i = \sum_T w_T \sum_T H_{T,i}$, where w_T is the tissue weighting factor, “that approximates its relative contribution to the overall detriment from uniform whole-body irradiation by sparsely ionising radiation” (Harrison et al., 2021b). So, E_i is the effective dose, also in units of sieverts, integrated for the segment i -esim of the flight track. This process is repeated for each segment of the track, and the total effective dose is then calculated by summation, $E = \sum_i^{N-1} E_i$, and the same for D , H and B_R , where B_R is just the integrated number of secondary particles per radiation type.

3. Results

To test the effectiveness of ACORDE, the total effective dose received in more than 300 flights was calculated by using the above described methodology. As mentioned, the dose for the same flights was also calculated using CARI7-A with the standard configuration and using the same path that was used to perform ACORDE calculations to reduce the source of possible differences. Most of the studied flights in this work are from Iberia, IATA call sign IB, as it operates mainly within Spain and several international destinations in Europe and America, with some particular flights operated by Iberia under the call sign of Finnair (AY). For the dates included in this study, Iberia flights to and from Asia were suspended due to the COVID-19 pandemic. Thus, additional flights operated by Japan Airlines, IATA call sign JL, and Cathay Pacific, IATA call sign CX, were also included for studies on tracks related to geomagnetic disturbances due to Solar Activity that could affect the dose during a near-pole flight. It is obvious to mention that this methodology can be extended to any airline, route, and date.

⁴ Currently, γ , e^\pm , μ^\pm , n , p , α , other nuclei and other hadrons.

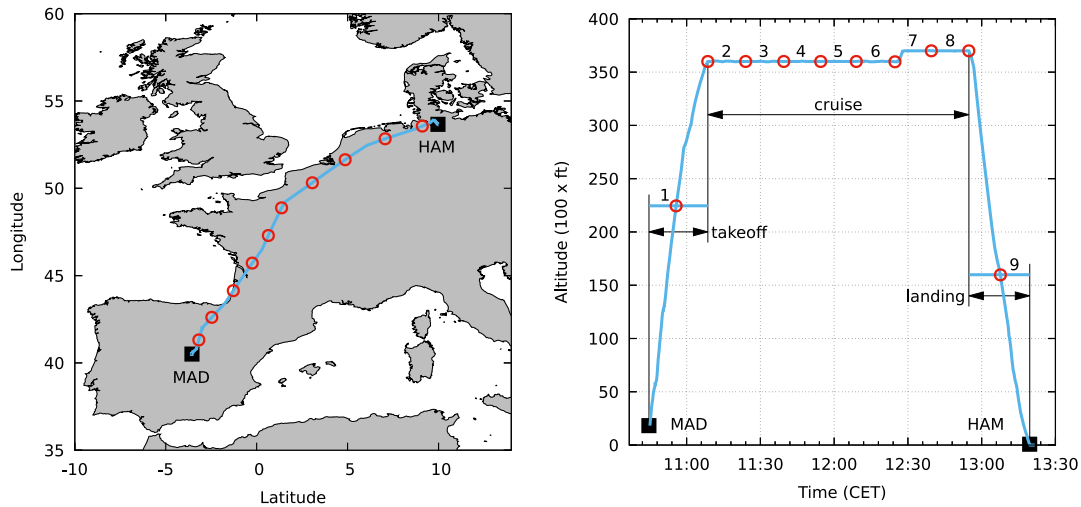


Fig. 1. Left: Real track (light blue line) of the flight IB3270 that flew from MAD to HAM (black squares) on 11/16/2021. ACORDE determined the start and the end of the cruise stage and calculated the waypoints where the dose had to be calculated (red circles). Right: Airplane altitude as a function of time (light blue line) and the waypoints (red circles) automatically identified by ACORDE as well as the three stages of the track: takeoff, cruise, and landing. For this calculation it is assumed that the altitude for the takeoff and the landing are the ones at the half time of the corresponding stage. The numbers corresponds to the segments where the onboard dose was calculated.

3.1. A complete example on how ACORDE performs

To better illustrate the way in which the results have been obtained with a specific example, let us consider the flight IB3270_20211116 operated by Iberia and flying from the Madrid Barajas Airport (MAD) to the Hamburg Airport (HAM) in an Airbus A320 (A320-216 EC-LXQ). The flight reported departure and arrival times at 11:43:50 CET and 14:20:46 CET respectively, with a total duration of 2 h 36 m 56 s (9416 s). However, according to the flight track, the actual takeoff and landing occurred at $t_0 = 11/16/2021 \ 10 : 44 : 40$ CET and $t_f = 11/16/2021 \ 14 : 19 : 31$ CET respectively, for a total duration of $\Delta t = 9,291$ s. ACORDE determined that the cruise altitude ($h_2 = 36,000$ ft for the first segment) was reached at $\Delta t_t = 1,375$ s after the takeoff, and the cruise duration was of $t_c = 6,370$ s. As this is an intermediate flight, the duration of each segment was adjusted to $\Delta t_i = 910$ s (15 m 10 s), resulting in $N = 10$ waypoints (eight for the cruise, including the corresponding starting and ending cruise waypoints, and 2 at the intermediate points of the takeoff and landing stages) and 9 segments where the dose was calculated. For this flight, the coverage factor was set to $\kappa = 6$, so the total flux integration time for each segment was $\tau_i = 5,460$ s. The flight track and the determined waypoints of the flight are shown in Fig. 1.

Once the waypoints were identified, the atmospheric profiles at \vec{r}_i are extracted from the GDAS database, and the Linsley's model is used to obtain the coefficients a_i , b_i and c_i , and the transition altitude h_i of each of the five atmospheric layers. With them, the atmospheric profiles are characterised and the density $\rho(h)$ and the mass overburden $X(h)$ as a function of the altitude are obtained. In Fig. 2, the reconstructed $X(h)$ for the seven segments of the cruise stage of the flight IB3270_20211116 are shown as well as the US standard model typically used as the reference for this kind of calculations. Slightly but important differences can be observed between the different local profiles bearing in mind the effect on the development of the atmospheric radiation Ξ_i is not only local, but mainly depends on the integral from the top of the atmosphere to the altitude of the segment. Moreover, the differences are largely increased when each of these profiles are compared with the standard atmospheric profile: at $h = 37,000$ the difference between X_2 and X_{Std} is of $12.5 \text{ g cm}^{-2} \approx 1.3 \text{ kPa}$ ($\sim 5\%$), and this kind of differences can be of more than 10% for near-polar flights (Dasso et al., 2016). No significant geomagnetic disturbances were observed during the flight, so the secular values of the geomagnetic field as well as the local rigidity cutoff tensor were calculated using only the IGRF-13 as explained in Asorey et al. (2018).

ACORDE collected and prepared all this information, and it was used within the ARTI docker to calculate the flux of expected secondary particles along each flight segment Ξ_i within the current energy ranges. While the flux is dominated by electromagnetic particles, when considering the dose this may not be the case taking into account the RBE for each type of particle. In the right panel of Fig. 3 the evolution of $\Xi_{i,j}$ along the flight track is shown for the different types of particles j : photons and electrons, muons, neutrons and nuclei and other hadrons, and also the secondary momentum distribution of Ξ_1 (takeoff) and Ξ_2 (cruise first segment) are shown as well as the integrated value of $\Xi_{i,j}$ for each flight segment and type of particle. It is clearly visible the altitude effect on Ξ_i , both in terms of atmospheric absorption and in the development of the EAS, with up to more than two orders of magnitude in the neutron flux when compared with similar spectra at ground level. As an example, the flux of particles at ground level typically ranges between 700 and $2000 \text{ m}^{-2} \text{ s}^{-1}$ within this energy range (Sarmiento-Cano et al., 2022), while the average flux of particles impinging this particular flight was of $65,000 \text{ m}^{-2} \text{ s}^{-1}$ and reached the maximum value of $93,000 \text{ m}^{-2} \text{ s}^{-1}$ for the segment $i = 8$. The total figures are also impressive: during the flight, among others, about 3700 n and 1200 p with $E > 50$ MeV, and $50,000$ γ s and 5400 e^\pm with $E > 50$ keV impinge each cm^2 of the aircraft and interacted with the fuselage, the avionics, and the people inside the plane.

Once the secondaries for each segment were obtained, the DOSE docker is deployed and the file containing Ξ was injected to calculate and integrate the effective dose for each segment, following the procedure according to the ICRP 103 recommendations (Valentin, 2007) and using an adapted implementation of the standard ICRP110 adult phantoms included in Geant4 (Large et al., 2020) as described in Section 2.2. Hence, the total effective dose for this flight obtained with the ACORDE framework was of $E_A = 11.6 \mu\text{Sv}$. As mentioned, ACORDE also produces a waypoint file compatible with CARI7-A, so the latter was used to also obtain a reference dose for each flight. In this case, the dose calculated by CARI7-A in the standard configuration was $E_C = 9.2 \mu\text{Sv}$. So, the observed differences in the calculated dose between ACORDE and CARI7-A are $\Delta E = E_A - E_C = 2.4 \mu\text{Sv}$ and $\Delta E\% = 2(E_A - E_C) / (E_A + E_C) = +23\%$ for this particular flight.

3.2. Extended analysis

All the described calculations were performed for 287 randomly selected flights operated by Iberia, plus 37 specific flights operated by

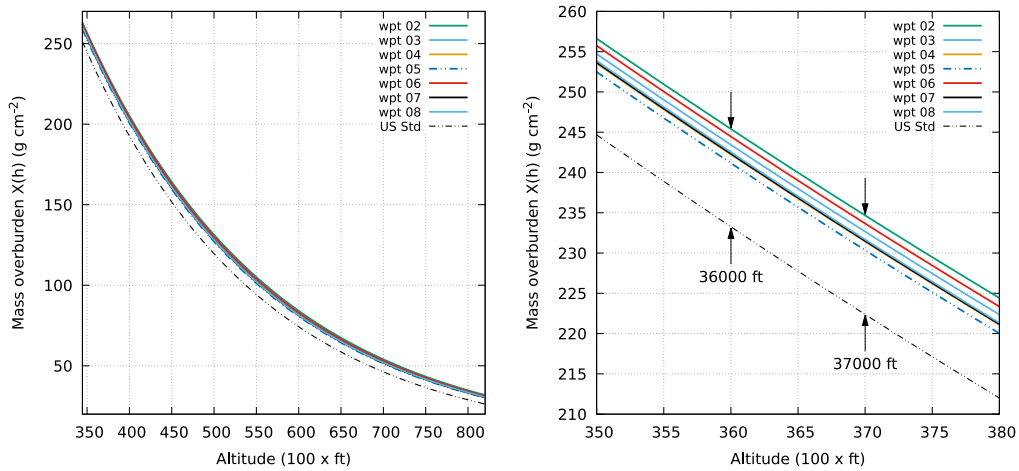


Fig. 2. The atmospheric mass overburden $X(h)$ as a function of the altitude h for the seven cruise segments of the flight IB3270 of 11/16/2021, between levels 350 and 800 (left) and at flight altitude (right). It was obtained from the atmospheric profiles extracted from the GDAS database. For comparative reasons, the mass overburden of the US Standard atmosphere is also shown. The observed difference between the locals and the US standard atmospheric profiles at the flight altitudes is of ~ 1.3 kPa ($\sim 5\%$).

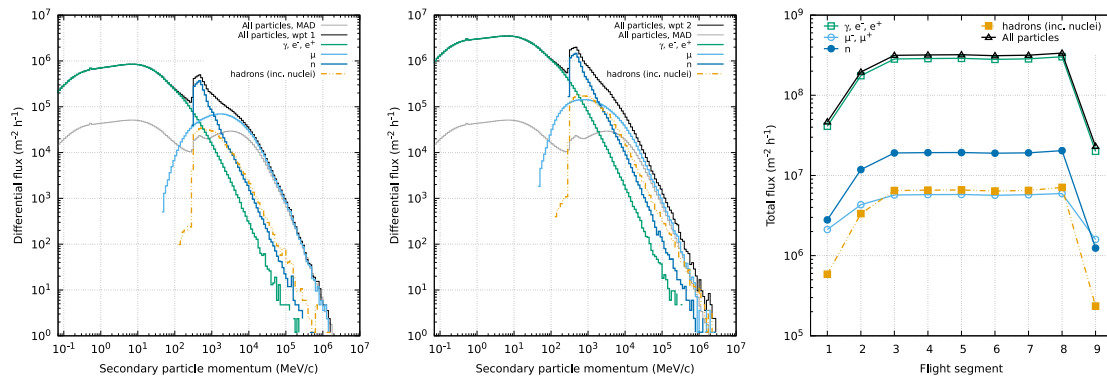


Fig. 3. The momentum spectrum of the secondary particles p_s that are expected for the flight IB3270_20211116 during the takeoff segment at an altitude of 22,450 ft (left), and during the first cruise segment $\vec{r}_2 \rightarrow \vec{r}_3$ at an altitude of 36,000 ft (centre). The electromagnetic component (dashed green line), the muons μ^\pm (dotted light blue line), neutrons (dashed dot blue line), and other hadrons including nuclei (double-dot dashed yellow line) are identifiable by their own characteristics (see Section 2). The altitude effect on the flux of the different components is clearly visible by comparing with the corresponding distribution for the total differential flux at MAD (grey solid line). The evolution of the integrated flux along the flight is shown on the right-hand side for the different components as well as for the total flux.

Japan Airlines, and Cathay Pacific that were selected to evaluate the ACORDE performance during a solar activity period, as described in Section 3.4. The obtained results are provided as a set of “tab separated values files” (.tsv) as supplementary material for this article (Asorey et al., 2022). In this section we provide a comparative analysis of the whole dataset. However, it is important to recall that each flight should be considered essentially unique, as even for the same route, the real track could be modified by meteorological reasons, crowded routes or operative reasons, and these alterations could have a significant impact on the total dose, especially for changes related to the flight altitude as it will be described in Section 3.5. Even more, local changes in the atmospheric and geomagnetic conditions, or the usage of a different aircraft vessel, could have a significant impact on the internal secondary particles distribution and the corresponding effective onboard dose. While all these factors are considered in most of the dose calculation codes including ACORDE, they can be assessed in different ways and could then produce different final results.

As explained in Section 2.2, all the analysed flights were separated into three categories depending on the flight duration, and labelled as 1, 2 and 3 for short, intermediate, and long flights respectively. As it is shown in Fig. 4 and in Table 1, when comparing the obtained values for E_A and E_C within each category some systematic differences raised. While it is important to remark that this comparative averaged

analyses is limited for the above described reasons, for the three categories the differences between the doses calculated by ACORDE are, in average, larger than the ones calculated with CARI7-A, in particular for long flights. For short and intermediate flights, the averaged absolute differences are compatible with zero within 1-sigma confidence interval. However, while the absolute differences are in the range $[-1.3, 1.9] \mu\text{Sv}$ and $[-4.0, 8.6] \mu\text{Sv}$ for short and intermediate flights, the observed relative differences could reach up to +50% and +70% in these categories when comparing the dose obtained by ACORDE with the one obtained using the same waypoints in the standard configuration of CARI7-A. The systematic differences are enlarged for the long range flights, where we observed a significant absolute excess of $\langle \Delta E \rangle = (+30.1 \pm 22.1) \mu\text{Sv}$ and relative $\langle \Delta E\% \rangle = (+43.5 \pm 36.5)\%$, with the doses observed ranges between $-19 \mu\text{Sv}$ and $+64.5 \mu\text{Sv}$ for the same absolute differences, and relative differences between -50.7% and 101.8% . However, when the 37 special flights are separated from the rest of the 287 flights, the observed average absolute difference in these long flights is reduced, as it can be seen in the last rows of Table 1 (types 3 for the 113 long flights analysed, 3^\ddagger correspond to the 37 special flights and 3^\dagger stands for the remaining 76 flights respectively) and is explained in the next subsection.

When analysing the observed differences, it is important to emphasise the level of detail that has been achieved in the ACORDE

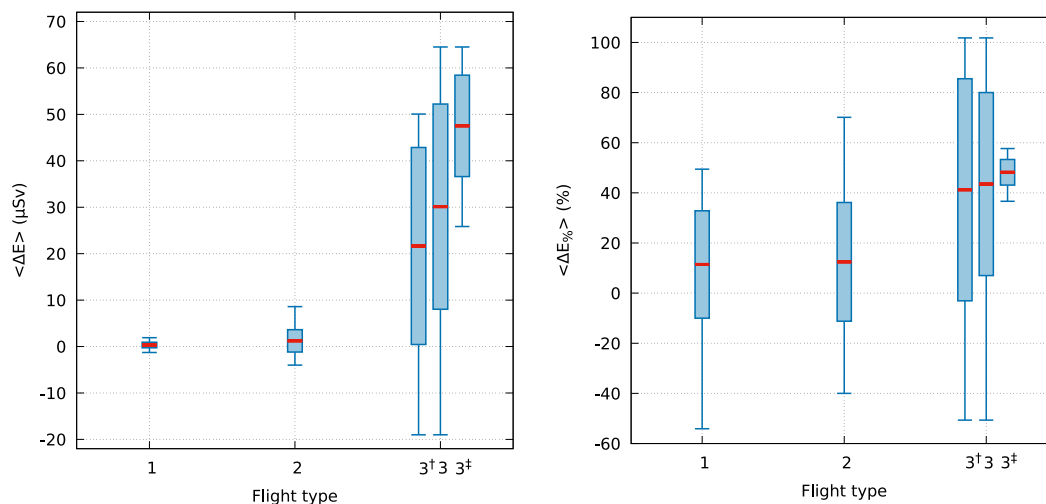


Fig. 4. Absolute $\langle \Delta E \rangle$ and relative $\langle \Delta E_{\%} \rangle$ averaged differences for the three studied flight categories and long flights subsets as described in the text and in Table 1. Candlesticks show the observed range and 1-sigma deviation from the mean (red line) of the corresponding differences (for the sake of clarity, the 3[†] and 3[‡] candlesticks were slightly displaced).

Table 1

Average differences between the total effective doses calculated with ACORDE, E_A , and CARI7-A, E_C , for the three flight categories described in the text: short (1), intermediate (2), and long (3) flights. The average absolute differences, $\langle \Delta E \rangle = \langle E_A - E_C \rangle$, and the corresponding relative differences, $\langle \Delta E_{\%} \rangle = \langle 2(E_A - E_C) / (E_A + E_C) \rangle \%$, are expressed in units of μSv and percents respectively, as well as the observed extrema of both magnitudes. For producing the last two rows (3[†] and 3[‡]), the 37 long (type 3) routes described in Section 3.4 were calculated apart to evidence the impact of these particular flights. Q stands for the number of flights averaged within each category. A graphic representation of this table can be seen in Fig. 4.

Type	Q	$\langle \Delta E \rangle$	ΔE range	$\langle \Delta E_{\%} \rangle$	$\Delta E_{\%}$ range
1	153	(0.3 ± 0.6)	$[-1.3, 1.9]$	$(11.4 \pm 21.4)\%$	$[-54.1\%, 49.4\%]$
2	58	(1.2 ± 2.4)	$[-4.0, 8.6]$	$(12.5 \pm 23.7)\%$	$[-40.0\%, 70.1\%]$
3	113	(30.1 ± 22.1)	$[-19.0, 64.5]$	$(43.5 \pm 36.5)\%$	$[-50.7\%, 101.8\%]$
3 [†]	76	(21.7 ± 21.2)	$[-19.0, 50.1]$	$(41.2 \pm 44.3)\%$	$[-50.7\%, 101.8\%]$
3 [‡]	37	(47.5 ± 10.9)	$[25.8, 64.5]$	$(48.2 \pm 5.1)\%$	$[36.6\%, 57.7\%]$

calculations, as it includes several important factors that could contribute to the dose in a flight-by-flight level, such as the use of the best available atmospheric conditions at the time of the flight for each segment of the route (see, e.g., Fig. 2), or the detailed model of the aircraft fuselage (see, e.g., Section 2.2), or the exact route that the plane travelled (see, e.g., Fig. 1), including important altitude changes (see, e.g., Section 3.5). These factors could largely affect the calculated dose when compared with methods based on interpolations or extrapolations of precompiled averaged libraries prepared under certain and well known conditions. On the other hand, being a method entirely based on Monte Carlo calculations, the stochastic nature of the critical steps of ACORDE’s methodology could introduce important fluctuations in the single calculation basis. However, and for this reason, it has been considered several constrains tending to control such fluctuations, such as the coverage factor κ described in Section 2.2. Moreover, it has been observed differences of >70% between the doses calculated by using only CARI7-A for the same commercial route, when the real path for each particular flight is considered. Nevertheless, as it was stressed at the beginning of this section, each flight should be considered as unique given the particular conditions that could affect the determination of the total dose. And finally, while ACORDE’s methodology relies in the existent experimental verifications of the implemented methods and codes at each step, such as CORSIKA, ARTI, Geant4 and the ICRP110 adult voxelized phantoms, it is also important to recall that the overall methodology was not still experimentally validated as a whole under field conditions by comparing ACORDE’s results with measurements

performed on board of the calculated flights. For this reason, it was included in ACORDE an additional module for the calculation of the doses that could be expected to be measured in some commercial detectors in a flight-by-flight basis and under the same conditions as the main ACORDE’s dose calculation.

3.3. Paving the way for a future experimental verification of ACORDE

As mentioned in Section 2, ACORDE includes a module for the simulation of the expected doses that can be registered by a Gamma-Scout (Gamma-Scout GmbH, 2022) installed onboard the aircraft and placed in close contact with the internal surface of the cabin. The Gamma-Scout is a dosimeter that is actively used in several industries to determine environmental radioactive doses. It allows the measurement of α -, β - and γ -radiation thanks to an LND end-window⁵ cylindrical counting Geiger–Müller (GM) tube of 9.1 mm in diameter and 38.1 mm in length. Without shielding, it is able to measure α s with $E_{\alpha} > 4$ MeV, electrons with $E_e > 200$ keV, and photons with $E_{\gamma} > 30$ keV. A special mechanical selector can be used to place an aluminium sheet of 3 mm thick to block all the α particles and electrons with $E_e < 2$ MeV, an aluminium foil of 0.1 mm thick shielding only the α -radiation, or leave the window open for simultaneously measuring the three types of radiation. For defining the calibration constants of the simulated device only the tube was simulated and it is assumed the detector is operated with the measurement windows totally open. As for the calibration of the physical device, we simulate three different sources of ¹³⁷Cs, ⁶⁰Co, ^{99m}Tc, and ¹⁸F sources with an spherical emission placed at 1 m in air of the simulated device in the open window configuration and adjusted the corresponding calibration constants of the Metropolis Monte Carlo algorithm up to obtaining the figures reported in pages 68–69 of Gamma-Scout GmbH (2022). For example, an effective dose rate of $86 \mu\text{Sv h}^{-1}$ for the 1 GBq ¹³⁷Cs source was obtained. Once the calibration parameters were obtained, we irradiated the simulated dosimeter in the open configuration with photons of $E_{\gamma} = 662$ keV (¹³⁷Cs) and observed that a rate of 150 CPM (counts per minute) corresponded to an effective dose rate of $1 \mu\text{Sv h}^{-1}$ (please see page 43 of Gamma-Scout GmbH (2022)). Thus, once the simulated detector is properly calibrated, we are able to estimate the expected dose rate for each

⁵ Typically made of muscovite (mica), with $X \approx 1.5\text{--}2 \times 10^{-3} \text{ g cm}^{-2}$ and simulated as a mixtures of 50% of SiO₂, 35% of Al₂O₃, 10% of K₂O, 4% of Fe₂O₃ and 1% of Na₂O.

Table 2

Expected effective doses calculated by using ACORDE and CARI7-A for some selected flights, including the expected dose as it should be measured by a Gamma-Scout (GS) device onboard the aircraft close to the internal surface of the cabin. Total effective doses are expressed in units of μSv .

T	Flight	Date	E_A	E_C	GS	T	Flight	Date	E_A	E_C	GS
2	IB3058	20210903	12.5	11.5	5.2	3	IB6177	20211211	100.1	68.0	49.1
2	IB3059	20210903	11.5	10.8	4.2	3	IB6178	20211212	93.9	63.6	49.8
3	CX0843	20211024	126.0	78.1	43.7	3	IB6250	20210904	42.5	30.4	17.9
3	CX0844	20211024	130.2	77.8	48.0	3	IB6251	20210901	45.0	33.4	19.0
3	IB6011	20211128	45.4	33.1	26.2	3	IB6453	20210707	33.0	41.0	19.8
3	IB6012	20211130	47.9	32.5	28.0	3	IB6454	20210709	32.0	40.0	18.0

segment of the flight and the total integrated dose. So from the flux of atmospheric radiation at each segment, we select only γ , e^\pm and α within the corresponding energy range⁶ and the detector calibration take place by using the same DOSE docker as for the effective dose in humans. In the Table 2 the obtained doses are shown for some selected flights. It is important to notice that both ACORDE and CARI7-A estimate the effective doses by using the response to all the radiation present in the atmospheric radiation. However, as any other GM tube (where the measurement of the energetic particles detection is strongly suppressed) neutrons are not detected since these particles does not ionise the gas. For these reasons, the total dose measured by a Gamma-Scout or any similar device will be lower than the dose calculated by considering all the atmospheric radiation effects including muons, energetic particles and specially neutrons. By design, ACORDE is able to predict the expected dose that a commercial GM based dosimeter could measure onboard the aircraft in exactly the same circumstances as the total effective dose is determined, opening an easy way to test ACORDE predictions by following a standard procedure in the aviation industry and avoiding the necessity of installing other types of detectors that could affect the normal operation of the flight (despite they are a much more precise way that determine the total effective dose than a simple commercial GM-based dosimeter).

Summarising, it will be easy to experimentally estimate if ACORDE provides accurate results by comparing the values simulated with this code running under the Gamma-Scout module (labelled as GS in Table 2) and a real measurement with any present-day Gamma-Scout detector installed in an airplane. Might this hypothesis be confirmed, it could be derived that the ACORDE estimation of the dose absorbed taking into account only the α -, β - and γ -radiation (GS again) is correct and, consequently, the estimation of ACORDE under the module which takes into account the whole spectrum of radiation (E_A) will be potentially valid as well.

3.4. Analysis of some long West–East–West flights

Between the end of October and the beginning of November 2021, a period of high solar activity was reported after the solar active region identified as NOAA 2887 produced some M-class flares and an X1 flare on Oct 28th, hence generating the ground level enhancement GLE73 with some geomagnetic storms recorded on Octst, and releasing a slow interplanetary coronal mass ejection (iCME) pointing to Earth on Nov 1st. A few hours later, the NOA 2891 active region produced a fast iCME that also pointed to Earth and interacted in the interplanetary space with the slower NOAA 2887 iCME resulting into a complex structure that arrived to Earth on November 3rd at 19:24 UTC, producing geomagnetic disturbances with observed DST (disturbance storm index) (Dessler and Parker, 1959) of -5 nT. The reader is referred to the work by Li et al. (2022) about the complex interactions observed. To evaluate the ACORDE performance during these particular events, 37 particular flights that flew between October 22nd, 2021 and November 21st, 2021 have been studied. Thus, these particular routes were affected by the aforementioned high solar activity: CX843 (JFK-HKG),

CX829 (YYZ-HKG), JL42 (LHR-HND) in the Europe to Asia direction, and CX844 (HKG-JFK), CX826 (HKG-YYZ) and JL41 (HND-LHR) in the reverse one. In the type 3[‡] row of the Table 1, the comparative analysis between the doses calculated with ACORDE and CARI7-A are shown. Large absolute and relative average differences, $\langle \Delta E \rangle = (47.5 \pm 10.9) \mu\text{Sv}$ in the range $[25.8, 64.5] \mu\text{Sv}$, and $\max(\Delta E\%) = (48.2 \pm 5.1)\%$ in the range $[36.6, 57.7]\%$ between both methods for these 37 flights can be observed. In Fig. 5, the time evolution of both the calculated doses with ACORDE and CARI7-A are shown for the studied routes. As mentioned in the Section 3.2, the geomagnetic disturbances, tracks, cruise altitude, and atmospheric conditions change from flight to flight even for the same routes. However, while important positive differences are observed between ACORDE and CARI7-A, which are even larger when this solar activity reaches the Earth, the global evolution within each route is approximately preserved. The table containing all the information of these flights is included in the supplementary material of this work (Asorey et al., 2022).

3.5. Impact of the cruise altitude in the total dose

While the atmospheric and geomagnetic conditions could produce measurable changes in the calculated values of the doses in the aircraft, the most important effect is related to changes in the cruise altitude during the flight. As an example of the ACORDE capabilities for calculating the dose in different conditions, we evaluate the evolution of the dose as a function of the altitude both in ACORDE and in CARI7-A by artificially changing the cruise altitude between 30,000 ft and 44,000 ft in steps of 2000 ft for the flights IB6177_20211211 (MAD-LAX) and IB6178_20211212 (LAX-MAD). The rest of the conditions of both flights and the selected waypoints were preserved to avoid other possible sources of variations. In Fig. 6 the recorded track and the waypoints used for the track completion are shown for the original recorded and the modified tracks. It is clearly visible the different evolution of both flights: while the IB6178 remained at a constant altitude of 39,000 ft for almost all the cruise stages, the IB6177 altitude had some changes along its track.

Fig. 7 and Table 3 summarise the results of this altitude variation study. It is clearly noticeable the altitude effect on the total effective dose calculated both in ACORDE and in CARI7-A. Important differences, of up to a factor of more than 3, can be observed for both flights in the reconstructed doses when comparing their value as the altitude changes between 30,000 ft and 44,000 ft, the current maximum altitude that the new generation of airplanes can reach.

3.6. ACORDE computing performance

As mentioned in Section 2.2, ACORDE relies on a large amount of computing power to perform the described Monte Carlo simulations on a flight-by-flight basis. For this reason, the codes are prepared to run within docker containers that can be deployed in high-performance computing facilities, small clusters running at Universities, and distributed environments running on public clouds, such as AWS or Google Cloud, and federated ones, such as the European Open Science Cloud (Rubio-Montero et al., 2021b). However, the code that controls the global execution of the calculations can run on a standard personal computer.

⁶ In this version of ACORDE, the lower energy limit for the simulated photons is 50 keV instead of 30 keV.

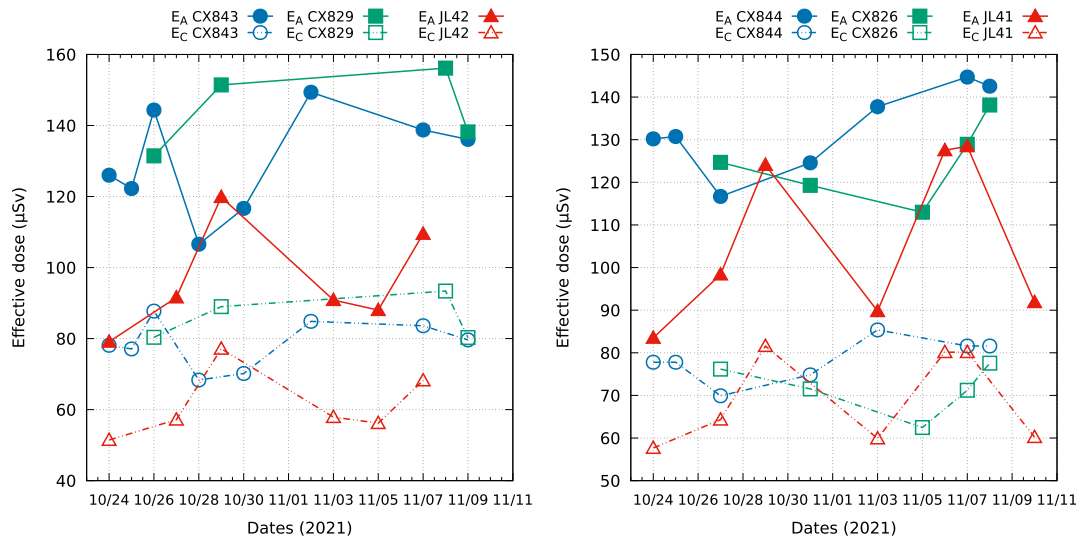


Fig. 5. Temporal evolution of the doses calculated by using ACORDE (filled symbols, dashed lines) and CARI7-A (empty symbols, dotted-dashed lines) for 37 flights covering routes between Europe to Asia (left) and Asia to Europe (right) during a high solar activity period by the end of October and the beginning of November 2021. It is important to notice that tracks, cruise altitudes, and the atmospheres varies from flight to flight, even for those serving the same route.

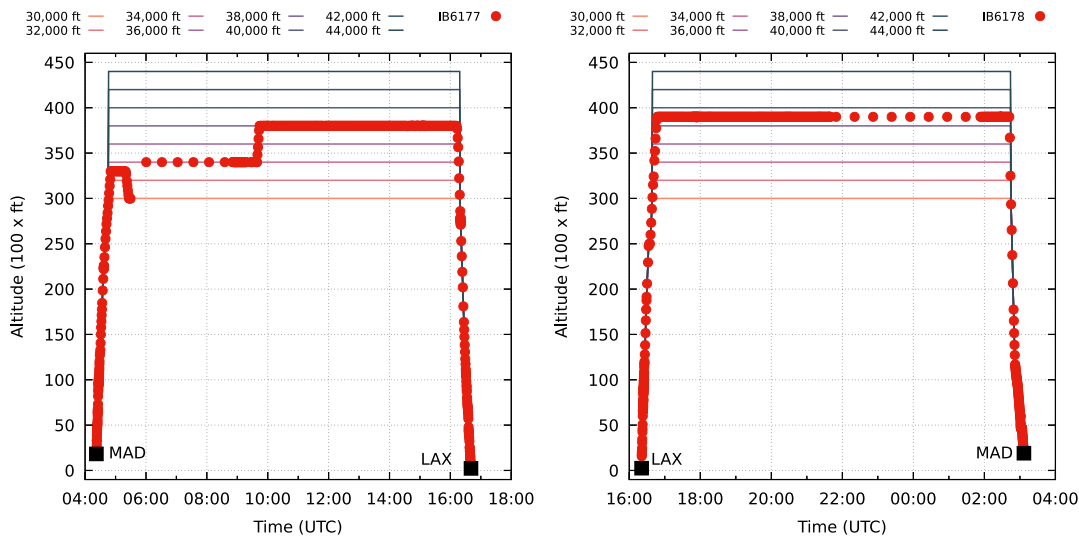


Fig. 6. Recorded and modified tracks for the flights IB6177 (MAD-LAX) and IB6178 (LAX-MAD) of December, 11th and 12th 2021. The original track (red circles) has been artificially modified to evaluate the effect of the altitude on the effective dose when all the other conditions remain unaltered, resulting in the tracks with cruise altitude from 30,000 ft to 44,000 ft every 2000 ft (coloured solid lines). The unrecorded segments of the cruise above the Atlantic ocean and the reconstructed path are noticeable at the beginning (IB6177) and ending (IB6178) of the tracks, as the waypoints are separated by $\Delta t_i = 1857$ s and $\Delta t_i = 1877$ s respectively.

Table 3

Cruise altitude effect over the total effective dose for both the studied flights IB6177 and IB6178. Important differences up to a factor of ≥ 3 in the dose can be observed between cruise altitude of 30,000 ft and 44,000 ft. The doses of the original flights are also included.

Flight	Date	Alt	E_A	E_C	Flight	Date	Alt	E_A	E_C
IB6177	20211211	orig	100.0	68.0	IB6178	20211212	orig	93.9	63.6
IB6177	20211211	30000	57.6	42.0	IB6178	20211212	30000	43.5	33.1
IB6177	20211211	32000	71.4	50.5	IB6178	20211212	32000	53.0	39.5
IB6177	20211211	34000	86.1	59.6	IB6178	20211212	34000	64.2	46.4
IB6177	20211211	36000	102.4	69.2	IB6178	20211212	36000	77.6	53.6
IB6177	20211211	38000	117.8	79.3	IB6178	20211212	38000	91.3	61.1
IB6177	20211211	40000	137.3	89.8	IB6178	20211212	40000	105.2	68.7
IB6177	20211211	42000	154.9	100.4	IB6178	20211212	42000	122.7	76.2
IB6177	20211211	44000	172.6	110.9	IB6178	20211212	44000	136.3	83.7

The calculation starts from a file containing the list of all the ACORDE flights codes that need to be calculated. ACORDE reads the file, identifies the corresponding flights, checks for their existence and the corresponding information in flight databases, and gathers all the related data to the flight, including the track. All the information is

combined to obtain the waypoints for the segmented track (both in ACORDE and CARI7-A format), and the instantaneous atmospheric profiles and geomagnetic conditions for each waypoint. The data is packed and transferred to either HPC or cloud-based facilities, where

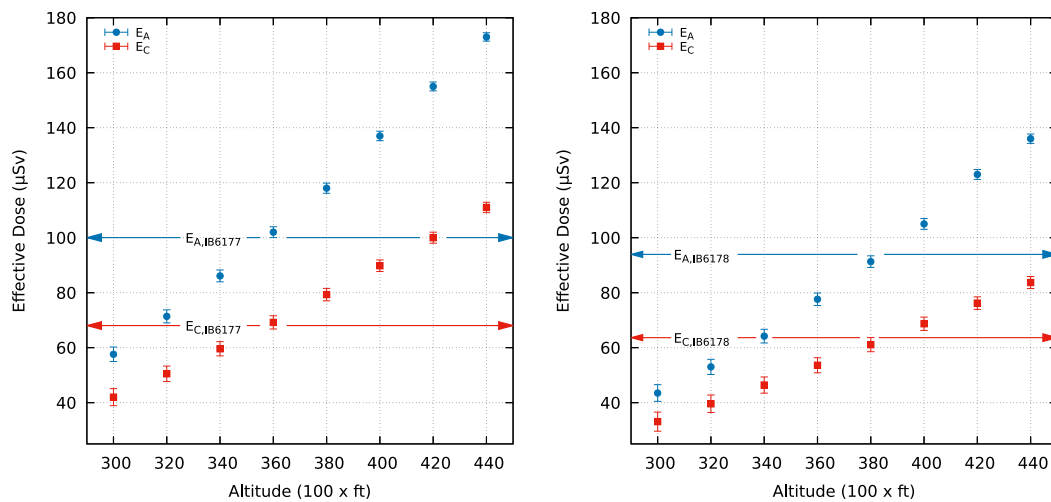


Fig. 7. Effective dose as a function of the cruise altitude of the modified flights IB6177 (MAD-LAX) and IB6178 (LAX-MAD) of December, 11th and 12th 2021, as it was determined by ACORDE (blue circles) and with the standard configuration of CARI7-A (red squares). As a reference, the doses calculated for the original flights are indicated by the respective arrows.

the dockers are deployed as described before, the Monte Carlo simulations start, and are further controlled by local daemons within the docker containers. The final result consists of a collection of different files containing all the required information, essentially, a JSON file containing lists with the values for the local E_i , H_i , D_i and $B_{R,i}$, the total values of all the doses E , H , D , B_R , and the dose calculated by CARI7-A using the standard configuration. All these files and the .DEG file, are then transferred back to the ACORDE main code for the final integration and preservation of the results. All the information needed to completely reproduce the calculation is securely stored for reproducibility matters. The larger files, such as those containing the secondaries reaching each waypoint, are also stored in a cloud storage for further analysis. While the overall file sizes will depend on the track conditions and the altitude changes during the flight, as a rule of thumb and on average, the simulation requires a total storage of about ≈ 6 GB per hour of flight of heavily compressed binary files. However, given that the showers files can be exactly recovered by re-running again the simulation using the same inputs as for the original calculation, the storage needs are largely reduced down to ≈ 1 MB per hour of flight of uncompressed files and ≈ 100 kB per hour when compressed. Regarding the computing power required, again it will also depend on the exact track (specially the altitude), and of course on the computing system used. In common HPC clusters running processors based on the Intel 6240 at 2.6 GHz and 100 Gb/s connection network, the total computation time, including the preliminaries, the EAS developments, and the dose calculations can be estimated as ~ 7 – 9 CPU-hours per hour of flight.

4. Conclusions and future perspectives

In this work, the methodology and capabilities of the *Application Code for the Radiation Dose Estimation* (ACORDE) are presented. ACORDE is a new code that integrates the current state-of-the-art Monte Carlo simulation codes for the interaction of cosmic rays with the atmosphere, in general for the interaction of radiation with matter, and for estimating the effective dose that the crew and passengers could receive being onboard of a commercial flight. By gathering the available information of the flight, including the real track of the plane, ACORDE identifies the main characteristics of the route and divides the track in segments of predefined duration. For each segment, the local atmospheric and geomagnetic conditions are determined and these data are then used to determine the flux of atmospheric radiation expected at each segment. Then, this flux is propagated in Geant4 models of the plane and an anthropomorphic phantom based on the Geant4

reference ICRP Adult voxel phantoms, to calculate the effective dose following the last ICRP recommendations (Harrison et al., 2021b). With ACORDE it is also possible to intentionally vary the track and altitude for comparative reasons, and to calculate the expected radiation that commercial dosimeters installed onboard the cabin would measure in exactly the same conditions as the total effective dose for the flight was calculated. As a reference, in this work the total dose for each analysed flight is also calculated with CARI7-A in the standard configuration and by using the same waypoints that were used to define the ACORDE segmentation.

To assay ACORDE capabilities, a total of 324 flights covering very different routes mainly starting from Spain were analysed. Accordingly, the flights are classified as short (< 2 h), intermediate (< 4 h) or long (> 4 h) flights based on their duration. In some flights very significant differences were observed between the doses calculated with ACORDE and CARI7-A, in particular for the case of long west–east–west routes. Moreover, ACORDE dose estimation is, on average, systematically larger than the corresponding CARI7-A effective dose, specially when constrained to the long flights category. While each flight should be considered essentially unique, the observed absolute and average differences between the effective dose calculated with ACORDE and CARI7-A remain and are compatible with zero within the systematic error bars in the three studied group. This is not the case when the 37 long west–east–west analysed routes that flew during an active Solar period are included. While ACORDE relies in the methodological integration of codes and techniques that were extensively validated multiple experiments and observatories, it still lack of an overall experimental validation of the calculated doses. By using ACORDE commercial dosimeters simulation capabilities, these discrepancies could be resolved by a flight-by-flight measurement campaign based on compact non-gaseous neutron detectors and commercial GM dosimeters as those regularly used in the industry.

Starting only from the list of flights to be analysed, the current version of ACORDE (1.0.0) is able to run on a single desktop computer and to command and control all the required simulations that could be performed on small local clusters or large HPC and cloud-based public and federated infrastructures in an autonomous and unsupervised way. Future versions of ACORDE will include several capability improvements, such as: the enhancement of the fuselage model including inner structural and internal elements that could slightly affect the total shielding (such as stringers or the hand luggage in the cabin); both the complete human male and female ICRP-110 phantoms; an extension based on CORSIKA and FLUKA of the atmospheric neutrons energy range down to the epi- and thermal energy ranges; and, the integration

of the blockchain technology for reproducibility and traceability of all the information collected and produced in all the calculation stages of ACORDE.

CRedit authorship contribution statement

Hernán Asorey: Writing – original draft, Visualization, Validation, Supervision, Software, Project administration, Methodology, Investigation, Formal analysis, Data curation, Conceptualization. **Mauricio Suárez-Durán:** Writing – original draft, Software, Methodology, Investigation, Formal analysis, Conceptualization. **Rafael Mayo-García:** Writing – original draft, Supervision, Project administration, Methodology, Investigation, Funding acquisition, Formal analysis, Conceptualization.

Declaration of competing interest

The authors declare that they have no known competing financial interests or personal relationships that could have appeared to influence the work reported in this paper.

Data availability

I have shared the link to our data at the manuscript.

Acknowledgements

This work was partially supported by the computing facilities provided by CIEMAT, Spain and hosted in the Extremadura Research Centre for Advanced Technologies (CETA-CIEMAT, Turgalium supercomputer) and the Moncloa campus in Madrid (Xula supercomputer), with European Regional Development Fund (ERDF) funds. It was also partially co-funded by the “European Open Science Cloud-Expanding Capacities by building Capabilities” (EOSC-SYNERGY) project by the European Commission’ Horizon 2020 RI Programme under Grant Agreement 857647 and by the Comunidad de Madrid CABAHLA-CM project, Spain (S2018/TCS-4423).

References

- Agostinelli, S., Allison, J., Amako, K., et al., 2003. Geant4—a simulation toolkit. *Nucl. Instrum. Methods Phys. Res. A* 506, 250–303. [http://dx.doi.org/10.1016/S0168-9002\(03\)01368-8](http://dx.doi.org/10.1016/S0168-9002(03)01368-8).
- Airbus, 2020. Airbus A320 Aircraft Characteristics Airport and Maintenance Planning. Airbus SAS, Blagnac, pp. 1–397, URL: <https://www.airbus.com/sites/g/files/jlcbta136/files/2021-11/Airbus-Commercial-Aircraft-AC-A320.pdf>.
- Airbus, 2021. Airbus a350 aircraft characteristics airport and maintenance planning. Airbus SAS, Blagnac, pp. 1–411, URL: <https://www.airbus.com/sites/g/files/jlcbta136/files/2021-11/Airbus-Commercial-Aircraft-AC-A350-900-1000.pdf>.
- Alken, P., Thébaud, E., Beggan, C.D., et al., 2021b. International geomagnetic reference field: the thirteenth generation. *Earth Planets Space* 73, 49. <http://dx.doi.org/10.1186/s40623-020-01288-x>, URL: <https://earth-planets-space.springeropen.com/articles/10.1186/s40623-020-01288-x>.
- Ambrožová, I., Beck, P., Benton, E.R., Billnert, R., Bottollier-Depois, J.-F., Caresana, M., Dinar, N., Domański, S., Gryziński, M.A., Kákona, M., Kolros, A., Krist, P., Kuc, M., Kyselová, D., Latocha, M., Leuschner, A., Lillhök, J., Maciak, M., Mareš, V., Łukasz Murawski, Pozzi, F., Reitz, G., Schennetten, K., Silari, M., Šlegl, J., Sommer, M., Štěpán, V., Trompier, F., Tscherne, C., Uchihoiri, Y., Vargas, A., Viererbl, L., Wielunski, M., Wising, M., Zorloni, G., Ploc, O., 2020. REFLECT – Research flight of EURADOS and CRREAT: Intercomparison of various radiation dosimeters onboard aircraft. *Radiat. Meas.* 137, 106433. <http://dx.doi.org/10.1016/j.radmeas.2020.106433>.
- Asorey, H., Dasso, S., Núñez, L., Pérez, Y., Sarmiento-Cano, C., Suárez-Durán, M., et al., 2015. The LAGO space weather program: Directional geomagnetic effects, background fluence calculations and multi-spectral data analysis. In: *The 34th International Cosmic Ray Conference*, Volume PoS(ICRC2015), Vol. 142. <http://dx.doi.org/10.22323/1.236.0142>.
- Asorey, H., Mayo-García, R., 2022. Calculation of the high-energy neutron flux for anticipating errors and recovery techniques in exascale supercomputer centres. *J. Supercomput.* <http://dx.doi.org/10.1007/s11227-022-04981-8>.
- Asorey, H., Núñez, L.A., Suárez-Durán, M., 2018. Preliminary results from the latin American giant observatory space weather simulation chain. *Space Weather* 16, 461–475. <http://dx.doi.org/10.1002/2017SW001774>.
- Asorey, H., Sarmiento-Cano, C., Suárez-Durán, M., Rubio-Montero, A.J., 2022a. The ARTI framework, github.com. <http://dx.doi.org/10.5281/zenodo.7316555>, URL: <https://github.com/lagoproject/arti>.
- Asorey, H., Suárez-Durán, M., Mayo-García, R., 2022. ACORDE: A new application for estimating the dose absorbed by passengers and crews in commercial flights (supplementary material). <http://dx.doi.org/10.5281/zenodo.7319773>.
- Bartlett, D.T., 2004. Radiation protection aspects of the cosmic radiation exposure of aircraft crew. *Radiat. Prot. Dosim.* 109, 349–355. <http://dx.doi.org/10.1093/rpd/nch311>.
- Battistoni, G., Boehlen, T., Cerutti, F., Chin, P.W., Esposito, L.S., Fassò, A., Ferrari, A., Lechner, A., Empl, A., Mairani, A., Mereghetti, A., Ortega, P.G., Ranft, J., Roesler, S., Sala, P.R., Vlachoudis, V., Smirnov, G., 2015. Overview of the FLUKA code. *Ann. Nucl. Energy* 82, 10–18. <http://dx.doi.org/10.1016/j.anucene.2014.11.007>.
- Beaujean, R., Kopp, J., Reitz, G., 1999. Radiation exposure in civil aircraft. *Radiat. Prot. Dosim.* 85, 287–290. <http://dx.doi.org/10.1093/oxfordjournals.rpd.a032853>.
- Bertolli, C.P., Sarmiento-Cano, C., Asorey, H., 2022. Estimación del flujo de muones en el laboratorio subterráneo andes. In: *ANALES AFA, Volume 32, No. 4*. pp. 106–111.
- Blümer, J., Engel, R., Hörandel, J.R., 2009. Cosmic rays from the knee to the highest energies. *Prog. Part. Nucl. Phys.* 63 (2), 293–338. <http://dx.doi.org/10.1016/j.pnpnp.2009.05.002>.
- Clarke, R.H., Dunster, C.H.J., Guskova, L.A.K., Jacobi, M.W., Li, N.D., Linecki, T.J., Meinhold, L.C.B., Mettler, U.F., Shigematsu, A.L., Silini, H.G., Sinclair, I.W.K., Lindell, B.B., Morgan, S.K.Z., Taylor, A.L.S., 1990. ICRP 60: The 1990 recommendations of the international commission on radiological protection. *Ann. Int. Comm. Radiol. Prot.* 21, 1–211. <http://dx.doi.org/10.1088/0952-4746/11/3/006>.
- Clement, C., 2009. ICRP 110: Adult reference computational phantoms. *Ann. Int. Comm. Radiol. Prot.* 39, 165, URL: <https://journals.sagepub.com/toc/anib/39/2>.
- Copeland, K., 2017. CARI-7A: Development and validation. *Radiat. Prot. Dosim.* 175, 419–431. <http://dx.doi.org/10.1093/rpd/ncw369>.
- Copeland, K., 2021. CARI Documentation: User’s Guide Final Report DOT/FAA/AM-21/6. Federal Aviation Administration, Oklahoma City, pp. 1–44, URL: https://www.faa.gov/data_research/research/med_humanfacfs/oamtechreports/2020s/media/202106.pdf.
- Dasso, S., Gulisano, A.M., Masías-Meza, J.J., Asorey, H., 2016. A project to install water-Cherenkov detectors in the Antarctic Peninsula as part of the LAGO detection network. In: *Proceedings of the 34th International Cosmic Ray Conference — PoS(ICRC2015)*. Sissa Medialab, Trieste, Italy, p. 105. <http://dx.doi.org/10.22323/1.236.0105>.
- Dawson, B.R., 2017. The importance of atmospheric monitoring at the Pierre Auger Observatory. *EPJ Web Conf.* 144, 01001. <http://dx.doi.org/10.1051/epjconf/201714401001>, URL: <http://www.epj-conferences.org/10.1051/epjconf/201714401001>.
- Desorgher, L., Büttikofer, R., Moser, M.R., 2003. Geant4 application for simulating the propagation of cosmic rays through the earth’s magnetosphere space radiation monitoring view project HESPERIA view project. In: *Proceedings of the 28th International Cosmic Ray Conference*. Universal Academy Press, Tsukuba, Japan, pp. 4281–4285, URL: <https://www.researchgate.net/publication/234240005>.
- Dessler, A.J., Parker, E.N., 1959. Hydromagnetic theory of geomagnetic storms. *J. Geophys. Res.* 64, 2239–2252. <http://dx.doi.org/10.1029/JZ064i012p02239>.
- Dyer, C., Lei, F., 2001. Monte Carlo calculations of the influence on aircraft radiation environments of structures and solar particle events. *IEEE Trans. Nucl. Sci.* 48, 1987–1995. <http://dx.doi.org/10.1109/23.983161>.
- Engel, R., Heck, D., Huege, T., Pierog, T., Reininghaus, M., Riehn, F., Ulrich, R., Unger, M., Veberič, D., 2019. Towards a next generation of CORSIKA: A framework for the simulation of particle cascades in astroparticle physics. *Comput. Softw. Big Sci.* 3, 2. <http://dx.doi.org/10.1007/s41781-018-0013-0>.
- Fesefeldt, H., 1985. The Simulation of Hadronic Showers - Physics and Applications - Report PITHA-85/02. Physikalisches Institut, Aachen, pp. 1–205, URL: <http://cds.cern.ch/record/162911/files/CM-P00055931.pdf>.
- Galindo, A., Moreno, E., Carrasco, E., et al., 2017. Calibration of a large water-Cherenkov detector at the Sierra Negra site of LAGO. *Nucl. Instrum. Methods Phys. Res. A* 861, 28–37. <http://dx.doi.org/10.1016/j.nima.2017.03.055>.
- Gamma-Scout GmbH, 2022. Gamma-scout. Measures radioactivity easily and reliably. URL: www.gamma-scout.com.
- Goldhagen, P., 2003. Cosmic-ray neutrons on the ground and in the atmosphere. *MRS Bull.* 28 (2), 131–135. <http://dx.doi.org/10.1557/mrs2003.41>.
- Greisen, K., 1960. Cosmic ray showers. *Annu. Rev. Nucl. Sci.* 10 (1), 63–108. <http://dx.doi.org/10.1146/annurev.ns.10.120160.000431>.
- Grieder, P.K.F., 2010. Extensive Air Showers and High Energy Phenomena. Springer Berlin Heidelberg, Berlin, Heidelberg, <http://dx.doi.org/10.1007/978-3-540-76941-5>.
- Grisales-Casadiagos, J., Sarmiento-Cano, C., Núñez, L.A., 2022. Impact of global data assimilation system atmospheric models on astroparticle showers. *Can. J. Phys.* 100 (3), 152–157. <http://dx.doi.org/10.1139/cjp-2020-0561>.

- Harrison, J., Balonov, M., Bochud, F., Martin, C., Menzel, H.-G., Ortiz-Lopez, P., Smith-Bindman, R., Simmonds, J., Wakeford, R., 2021a. ICRP 147: Use of dose quantities in radiological protection. *Ann. Int. Comm. Radiol. Prot.* 50, https://doi.org/10.1177/ANIB_50_1, URL: https://journals.sagepub.com/doi/pdf/10.1177/ANIB_50_1.
- Harrison, J.D., Balonov, M., Bochud, F., Martin, C.J., Menzel, H.-G., Smith-Bindman, R., Ortiz-López, P., Simmonds, J.R., Wakeford, R., 2021b. The use of dose quantities in radiological protection: ICRP publication 147 ann ICRP 50(1) 2021. *J. Radiol. Prot.* 41, 410–422. <http://dx.doi.org/10.1088/1361-6498/abe548>.
- Heck, D., Knapp, J., Capdevielle, J.N., Schatz, G., Thow, T., 1998. CORSIKA: A Monte Carlo code to simulate extensive air showers.
- Heck, D., Pierog, T., 2020. Extensive air shower simulation with CORSIKA: A user's guide (Version 7.7402).
- Kampert, K.-H., Watson, A.A., 2012. Extensive air showers and ultra high-energy cosmic rays: a historical review. *Eur. Phys. J. H* 37 (3), 359–412. <http://dx.doi.org/10.1140/epjh/e2012-30013-x>.
- Large, M.J., Malaroda, A., Petasacca, M., Rosenfeld, A.B., Guatelli, S., 2020. Modelling ICRP110 adult reference voxel phantoms for dosimetric applications: Development of a new Geant4 advanced example. *J. Phys. Conf. Ser.* 1662, <http://dx.doi.org/10.1088/1742-6596/1662/1/012021>.
- Li, X., Wang, Y., Guo, J., Lyu, S., 2022. Solar energetic particles produced during two fast coronal mass ejections. *Astrophys. J. Lett.* 928, L6. <http://dx.doi.org/10.3847/2041-8213/ac5b72>.
- Lindborg, L., Bartlett, D., Beck, P., McAulay, I., Schnuer, K., Schraube, H., Spurny, F., 2004. Cosmic radiation exposure of aircraft crew: compilation of measured and calculated data. *Radiat. Prot. Dosim.* 110, 417–422. <http://dx.doi.org/10.1093/rpd/nch232>.
- Matthews, J., 2005. A Heitler model of extensive air showers. *Astropart. Phys.* 22 (5–6), 387–397. <http://dx.doi.org/10.1016/j.astropartphys.2004.09.003>.
- Merkel, D., 2014. Docker: Lightweight linux containers for consistent development and deployment. *Linux J* 239, 1–2, URL: <http://www.docker.io>.
- Mertens, C.J., Kress, B.T., Wiltberger, M., Blattig, S.R., Slaba, T.S., Solomon, S.C., Engel, M., 2010. Geomagnetic influence on aircraft radiation exposure during a solar energetic particle event in October 2003. *Space Weather* 8, <http://dx.doi.org/10.1029/2009SW000487>.
- Mertens, C.J., Meier, M.M., Brown, S., Norman, R.B., Xu, X., 2013. NAIRAS aircraft radiation model development, dose climatology, and initial validation. *Space Weather* 11, 603–635. <http://dx.doi.org/10.1002/swe.20100>.
- National Aerospace Administration (NASA), National Oceanic and Atmospheric Administration (NOAA), US Air Force, 1976. US Standard Atmosphere 1976. NOAA Technical Report NOAA-S/T-76-1562, National Oceanic and Atmospheric Administration.
- NOAA Air Resources Laboratory (ARL), 2004. Global data assimilation system (GDAS1) archive information. URL: <http://ready.arl.noaa.gov/gdas1.php>.
- Ostapchenko, S., 2011. Monte Carlo treatment of hadronic interactions in enhanced Pomeron scheme: QGSJET-II model. *Phys. Rev. D* 83, 014018. <http://dx.doi.org/10.1103/PhysRevD.83.014018>.
- Paretzke, H.G., Heinrich, W., 1993. Radiation exposure and radiation risk in civil aircraft. *Radiat. Prot. Dosim.* 48, <http://dx.doi.org/10.1093/oxfordjournals.rpd.a081840>.
- Peña-Rodríguez, J., Núñez, L.A., Asorey, H., 2021. Characterization of the muography background using the Muon Telescope (MuTe). In: Proceedings of 40th International Conference on High Energy Physics, Volume PoS(ICHEP2020), No. 984. pp. 1–4. <http://dx.doi.org/10.22323/1.390.0984>.
- Peña-Rodríguez, J., Vesga-Ramírez, A., Vázquez-Ramírez, A., Suárez-Durán, M., de León-Barrios, R., Sierra-Porta, D., Calderón-Ardila, R., Pisco-Guavabe, J., Asorey, H., Sanabria-Gómez, J., et al., 2022. Muography in Colombia: simulation framework, instrumentation and data analysis. *J. Adv. Instrum. Sci.* 2022, <http://dx.doi.org/10.31526/jais.2022.271>, Jun 2022.
- Roesler, S., Heinrich, W., Schraube, H., 2002. Monte Carlo calculation of the radiation field at aircraft altitudes. *Radiat. Prot. Dosim.* 98, 367–388. <http://dx.doi.org/10.1093/oxfordjournals.rpd.a006728>.
- Rubio-Montero, A.J., Pagán-Muñoz, R., Mayo-García, R., Pardo-Díaz, A., Sidelnik, I., Asorey, H., 2021a. The EOCS-synergy cloud services implementation for the latin American giant observatory (LAGO). In: Proceedings of 37th International Cosmic Ray Conference — PoS(ICRC2021). Sissa Medialab, Trieste, Italy, p. 261. <http://dx.doi.org/10.22323/1.395.0261>.
- Rubio-Montero, A.J., Pagan-Munoz, R., Mayo-Garcia, R., Pardo-Diaz, A., Sidelnik, I., Asorey, H., 2021b. A novel cloud-based framework for standardized simulations in the Latin American giant observatory (LAGO). In: 2021 Winter Simulation Conference, Vol. 2021-December. WSC, IEEE, pp. 1–12. <http://dx.doi.org/10.1109/WSC52266.2021.9715360>.
- Sanlorenzo, M., Wehner, M.R., Linos, E., Kornak, J., Kainz, W., Posch, C., Vujic, I., Johnston, K., Gho, D., Monico, G., McGrath, J.T., Osella-Abate, S., Quaglino, P., Cleaver, J.E., Ortiz-Urda, S., 2015. The risk of melanoma in airline pilots and cabin crew. *JAMA Dermatol.* 151, 51. <http://dx.doi.org/10.1001/jamadermatol.2014.1077>.
- Sarmiento-Cano, C., Asorey, H., Sacahui, J., Otiniano, L., Sidelnik, I., 2021. The Latin American giant observatory (LAGO) capabilities for detecting Gamma ray bursts. In: Proceedings of 37th International Cosmic Ray Conference, Volume PoS(ICRC2021), No. 929. pp. 1–4. <http://dx.doi.org/10.22323/1.395.0929>.
- Sarmiento-Cano, C., Suárez-Durán, M., Calderón-Ardila, R., Vázquez-Ramírez, A., Jaimes-Motta, A., Núñez, L.A., Dasso, S., Sidelnik, I., Asorey, H., 2022. The ARTI framework: cosmic rays atmospheric background simulations. *Eur. Phys. J. C* 82, 1019. <http://dx.doi.org/10.1140/epjc/s10052-022-10883-z>, URL: <https://link.springer.com/10.1140/epjc/s10052-022-10883-z>.
- Sarmiento-Cano, C., Suárez-Durán, M., Vázquez Ramírez, A., Jaimes-Motta, A., Calderón-Ardila, R., Peña-Rodríguez, J., 2019. Modeling the LAGO's detectors response to secondary particles at ground level from the Antarctic to Mexico. In: Proceedings of 36th International Cosmic Ray Conference, Volume PoS(ICRC2019), No. 412. pp. 1–4. <http://dx.doi.org/10.22323/1.358.0412>.
- Schrewe, U.J., 1999. Radiation exposure monitoring in civil aircraft. *Nucl. Instrum. Methods Phys. Res. A* 422, 621–625. [http://dx.doi.org/10.1016/S0168-9002\(98\)00971-1](http://dx.doi.org/10.1016/S0168-9002(98)00971-1).
- Sidelnik, I., Asorey, H., for the LAGO Collaboration, 2017. LAGO: The Latin American giant observatory. *Nucl. Instrum. Methods Phys. Res. A* 876, 173–175. <http://dx.doi.org/10.1016/j.nima.2017.02.069>.
- Sidelnik, I., Asorey, H., Guarín, N., Durán, M.S., Berisso, M.G., Lipovetzky, J., Blostein, J.J., 2020a. Simulation of 500 MeV neutrons by using NaCl doped water Cherenkov detector. *Adv. Space Res.* 65 (9), 2216–2222. <http://dx.doi.org/10.1016/j.asr.2020.02.024>.
- Sidelnik, I., Asorey, H., Guarín, N., Durán, M.S., Bessia, F.A., Arnaldi, L.H., Berisso, M.G., Lipovetzky, J., Pérez, M., Haro, M.S., et al., 2020b. Neutron detection capabilities of water Cherenkov detectors. *Nucl. Instrum. Methods Phys. Res. A* 952, 161962. <http://dx.doi.org/10.1016/j.nima.2019.03.017>.
- Sidelnik, I., Asorey, H., Guarín, N., Durán, M.S., Lipovetzky, J., Arnaldi, L.H., Pérez, M., Haro, M.S., Berisso, M.G., Bessia, F.A., et al., 2020c. Enhancing neutron detection capabilities of a water Cherenkov detector. *Nucl. Instrum. Methods Phys. Res. A* 955, 163172. <http://dx.doi.org/10.1016/j.nima.2019.163172>.
- Silberberg, R., Tsao, C., 1990. Spallation processes and nuclear interaction products of cosmic rays. *Phys. Rep.* 191 (6), 351–408. [http://dx.doi.org/10.1016/0370-1573\(90\)90109-F](http://dx.doi.org/10.1016/0370-1573(90)90109-F).
- Taboada, A., Sarmiento-Cano, C., Sedoski, A., Asorey, H., 2022. Meiga, a dedicated framework used for muography applications. *J. Adv. Instrum. Sci.* 2022 (1), <http://dx.doi.org/10.31526/jais.2022.266>.
- The Pierre Auger Collaboration, 2012. Measurement of the proton-air cross section at $\sqrt{s} = 57$ TeV with the Pierre Auger Observatory. *Phys. Rev. Lett.* 109 (6), 062002.
- The Pierre Auger Collaboration, 2020a. Studies on the response of a water-cherenkov detector of the Pierre Auger Observatory to atmospheric muons using an RPC hodoscope. *J. Instrum.* 15 (09), P09002. <http://dx.doi.org/10.1088/1748-0221/15/09/P09002>.
- The Pierre Auger Collaboration, 2020b. The Pierre Auger Observatory and its upgrade. *Sci. Rev. End World* 1 (4), 8–33. <http://dx.doi.org/10.52712/sciencereviews.v1i4.31>.
- Valentin, J., 2007. ICRP 103: The 2007 recommendations of the international commission on radiological protection. *Ann. Int. Comm. Radiol. Prot.* 37, 1–339, URL: https://www.icrp.org/publication.asp?id=ICRP_Publication_103.
- Vázquez-Ramírez, A., Ariza-Gómez, M., Carrillo-Moreno, M., Baldovino-Medrano, V., Asorey, H., Núñez, L., 2021. Improvised explosive devices and cosmic rays. In: Proceedings of 37th International Cosmic Ray Conference, Volume PoS(ICRC2021), No. 480. pp. 1–4. <http://dx.doi.org/10.22323/1.395.0480>.
- Vázquez-Ramírez, A., Suárez-Durán, M., Jaimes-Motta, A., Calderón-Ardila, R., Peña-Rodríguez, J., Sánchez-Villafrales, J., Sanabria-Gómez, J., Asorey, H., Núñez, L., 2020. Simulated response of MuTe, a hybrid muon telescope. *J. Instrum.* 15 (08), P08004. <http://dx.doi.org/10.1088/1748-0221/15/08/P08004>.
- Vesga-Ramírez, A., Sanabria-Gómez, J., Sierra-Porta, D., Arana-Salinas, L., Asorey, H., Kudryavtsev, V., Calderón-Ardila, R., Núñez, L., 2021. Simulated annealing for volcano muography. *J. South Am. Earth Sci.* 109, 103248. <http://dx.doi.org/10.1016/j.jsames.2021.103248>.
- Vuković, B., Poje, M., Varga, M., Radolić, V., Miklavčić, I., Faj, D., Stanić, D., Planinić, J., 2010. Measurements of neutron radiation in aircraft. *Appl. Radiat. Isot.* 68, 2398–2402. <http://dx.doi.org/10.1016/j.apradiso.2010.06.017>.
- Wrixon, A.D., 2008. New ICRP recommendations. *J. Radiol. Prot.* 28, 161–168. <http://dx.doi.org/10.1088/0952-4746/28/2/R02>.
- Yoo, A.B., Jette, M.A., Grondona, M., 2003. SLURM: Simple linux utility for resource management. In: Workshop on Job Scheduling Strategies for Parallel Processing, Vol. 2003. Springer, Berlin, pp. 44–60. http://dx.doi.org/10.1007/10968987_3.